ACS APPLIED MATERIALS & INTERFACES

Research Article

www.acsami.org

Multifunctional Hybrid Nanopatches of Graphene Oxide and Gold Nanostars for Ultraefficient Photothermal Cancer Therapy

Saide Z. Nergiz, Naveen Gandra, Sirimuvva Tadepalli, and Srikanth Singamaneni*

Institute of Materials Science and Engineering, Department of Mechanical Engineering and Materials Science, Washington University in St. Louis, 1 Brookings Drive, St. Louis, Missouri 63130, United States

Supporting Information

ABSTRACT: Multifunctional hybrid nanomaterials with enhanced therapeutic efficiency at physiologically safe dosages for externally triggered, image-guided therapy are highly attractive for nanomedicine. Here, we demonstrate a novel class of multifunctional hybrid nanopatches comprised of graphene oxide (GO) and gold nanostars for enhanced photothermal effect and image-guided therapy. The hybrid nanopatches with tunable localized surface plasmon resonance into the near-infrared therapeutic window (650−900 nm) were realized using a biofriendly method that obviates the need for toxic shape-directing agents. Internalization of the intact nanopatches into epithelial breast cancer cells was confirmed by Raman imaging, transmission electron microscopy, and inductively coupled plasma mass spectrometry. It appears that the amphipathic nature and the large surface area of the graphene oxide enable it to serve as a soft, flexible, and biocompatible intracellular carrier for the in situ grown plasmonic nanostructures and provide long-term biocompatibility with extremely low cytotoxicity. Apart from a remarkably improved photothermal effect compared to that of either of the components at very low dosages of the hybrids (10 μg/mL GO) and using a low laser power (0.75 W cm^{-2}), the hybrid nanopatches exhibit strong Raman scattering, making them excellent candidates for bioimaging, diagnostics, and image-guided therapy applications.

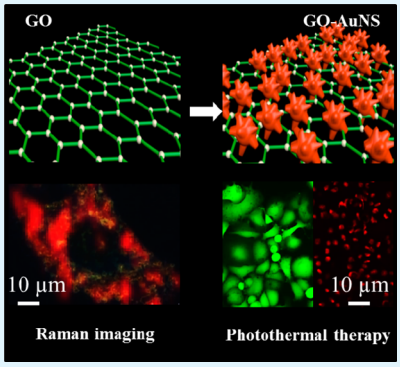

KEYWORDS: *photothermal therapy, gold nanostars, graphene oxide, surface-enhanced Raman scattering, Raman imaging*

1. INTRODUCTION

Hyperthermia is a promising approach for cancer therapy that can be performed at the local, regional, or whole-body level.[1] Nanomaterials that can efficiently absorb light and convert to heat are being extensively investigated as photothermal contrast agents for locoregional cancer therapy. Hyperthermia causes the denaturing of intracellular proteins and destroys critical cellular functions, thus resulting in necrotic or apoptotic cell death or sensitization to ionizing radiation or chemotherapy in combination therapies.[2] Hyperhermia-based therapy is of limited toxicity to most healthy tissues since tumor vasculature is prone to be more sensitive to the increased temperatures between 40 and 44 °C due to the difference in their environmental factors such as hypoxia and low pH compared to those of normal tissues. The magnitude and duration of heat can be adjusted on the basis of the thermotolerance of different types of cells and tissues to the thermal dose.[3,4]

Nanomaterials with optimal biophysicochemical characteristics promise revolutionary advances in diagnosis, imaging, and therapy of complex diseases such as cancer.[5−7] The unique physical and chemical properties such as a large absorption and scattering cross-section, high sensitivity to the local dielectric environment, and enhanced electric field at the surface make noble-metal nanostructures an important class of materials for nanomedicine.[8−10] Owing to their tunable localized surface plasmon resonance (LSPR) into the near-infrared region, various shape-controlled gold nanostructures such as shells, rods, cages, and hexapods have been extensively investigated, with some of these structures entering clinical trials.[11−15] More recently, graphene-based nanomaterials are being explored for nanomedicine applications which demonstrate favorable traits such as large surface area, potential biodegradability, biocompatibility, and low cytotoxicity.[16−21]

Realizing multifunctionality, for example, therapeutic ability combined with image contrast for image-guided therapy, with a single class of materials remains challenging.[22−24] Rational integration of diverse nanomaterials can synergistically enhance the efficacy and ameliorate current strategies to fight against complex diseases such as cancer.[25−27] Here we demonstrate the synthesis of multifunctional biocompatible graphene oxide (GO) and gold nanostar (AuNS) hybrids with excellent photothermal transduction capability at ultralow dosages that are well below the detected toxic level of the hybrids. An open sheet structure, the amphipathic surface chemistry, and the nanoscale flexibility of GO with gold nanostars anchored on their surface enhanced their colloidal stability and together with enabling cytosolic colocalization of the nanohybrids signifi-

Received: July 21, 2014
Accepted: August 25, 2014
Published: August 25, 2014

cantly improved the photothermal effect of the nanohybrids compared to either of the individual components.

2. EXPERIMENTAL SECTION

2.1. Synthesis of GO, AuNSs, and GO−AuNS Hybrids. GO layers were synthesized by oxidative exfoliation of graphite flakes according to a modified Hummer method.[28,29] The concentration and size of the GO layers was controlled by successive cycles of centrifugation and sonication. The graphene oxide sheets with lateral dimensions of ∼0.5 μm and a thickness of 1 nm (indicating that most of them are bilayers) was confirmed using atomic force microscopy (AFM) (Figure S1, Supporting Information). AuNSs have been synthesized using 4-(2-hydroxyethyl)-1-piperazineethanesulfonic acid (HEPES) as a reducing and shape-directing agent according to earlier work reported elsewhere with slight modifications.[30] Briefly, 2 μL of $HAuCl_4$ (0.1 M) was added to 1000 μL of 0.1 M HEPES at room temperature. Following the completion of the synthesis of the AuNSs, they were centrifuged at 10 krpm twice and redispersed in water. For GO−AuNS hybrid nanopatches, 5 μg/mL graphene oxide was added to 1200 μL of 0.1 M HEPES) followed by the addition of 2−12 μL of HAuCl4 (0.1 M). Subsequently, the GO−Au hybrids were centrifuged at 5000 rpm for 10 min to remove HEPES and any free gold nanostars and redispersed in water. The centrifugation procedure was repeated twice. The graphene to gold ratio was varied to tune the density, distribution, and LSPR band of the nanostructures. A GO−AuNS hybrid with an LSPR band at 802 ± 6 nm was used in this study. Unless stated otherwise, the GO and AuNSs were compared to the GO−AuNS hybrids at the same concentration to understand the biophysicochemical properties and the therapeutic effect of the hybrid structures compared to the individual components.

2.2. Characterization. Transmission electron microscopy (TEM) micrographs were obtained using a JEOL JEM-2100F field emission (FE) instrument. A drop of a sample in water was dried on a carbon-coated grid which had been made hydrophilic by glow discharge. AFM imaging was performed on a Dimension 3000 using silicon cantilevers with a nominal spring constant of 40 N/m in light tapping mode by maintaining the set point ratio greater than 0.9. A 10% (v/v) solution of (3-aminopropyl)triethoxysilane (APTES) in water was freshly prepared. Silicon substrates were immersed in APTES for 30 min followed by sonication in water for 60 min and dried under a stream of nitrogen. Graphene oxide and the GO−AuNS hybrid were coated on APTES-modified silicon by drop-casting for 30 min followed by thorough washing with water and drying under a stream of nitrogen. Raman spectra were collected by a Renishaw inVia confocal Raman spectrometer mounted on a Leica microscope with a 50× objective (NA = 0.75) using a 785 nm diode laser (0.5 mW). The spectra were obtained in the range of 400−2000 cm^{-1} with one accumulation and 10 s of exposure time. The extinction spectra of AuNSs and GO−AuNS hybrids were monitored by a Shimadzu UV-1800 spectrophotometer.

2.3. Cell Culture. Human epithelial breast cancer cells (SKBR-3) were purchased from ATCC (Manassas, VA) and subcultured in McCoy's 5A medium with 10% fetal bovine serum (FBS) and antibiotics (100 μg/mL penicillin and 100 μg/mL streptomycin) (Sigma). The cells were grown in a water jacket incubator at 37 °C with a 5% CO_2 humidified atmosphere in 25 cm^2 tissue culture flasks. Once the cells reached 90% confluence, they were washed with Dulbecco's phosphate-buffered saline (DPBS), detached with 2 mL of 0.25% trypsin−EDTA solution (Sigma), and then redispersed in 10 mL of complete medium. The cells were counted using a hemocytometer and plated at a density of 6.5 × 10^5 cells/mL on polylysine-coated 0.5 cm × 0.5 cm silicon substrates and 13 mm cover slides in a flat-bottom 24-well plate for Raman bioimaging and live imaging.

2.4. MTT (3-(4,5-Dimethylthiazol-2-yl)-2,5-diphenyltetrazolium Bromide) Assay. Cell viability was quantified by a colorimetric assay based on the mitochondrial oxidation of MTT using a cell proliferation kit (Roche). The cells were treated with 10 μL of freshly prepared MTT solution (5 mg/mL in DPBS) and incubated for an additional 4 h before treatment with 100 μL of dimethyl sulfoxide solubilization solution (Sigma). After 1 h, the absorbance of each well was measured using an ELISA plate reader (Spectra MAX 340, Molecular Devices) at an absorbance wavelength of 575 nm and a reference wavelength of 650 nm.

2.5. Inductively Coupled Plasma Mass Spectrometry (ICP-MS). To quantify the uptake of GO−AuNS hybrids by SKBR3 cells, ICP-MS (DRCII, PerkinElmer) was employed.[31] At the end of the intended incubation time of GO−AuNS hybrids with SKBR3 cells, the medium was removed and the cells were washed 3× with DPBS, trypsinized, and pelleted. A cell pellet that was treated with 3 mL of 1% HNO_3 was sonicated in a hot water bath for 30 min to disrupt the cell membranes followed by successive addition of 1 mL of 70 vol % HCl and 30 vol % HNO_3 and sonication for 1 h to completely dissolve Au. A commercial Au standard was used to obtain a calibration curve for the gold ions at various concentrations (1, 10, 50, 100, and 200 ppb).

2.6. In Vitro Raman Bioimaging. SKBR-3 cells plated on silicon substrates were rinsed two times with DPBS and incubated with 10 μg/mL GO−AuNS hybrids in complete medium for 24 h at 37 °C, maintaining above 90% viability. These cells were washed three times with DPBS and fixed with 4% formalin in DPBS for 20 min at room temperature. Then the fixed cells were washed three times with DPBS and permeabilized in 1% Triton. Finally, the fixed cells were located using a confocal InVia Renishaw Raman microscope under dark-field illumination. An array of Raman spectra were collected using a 785 nm wavelength diode laser as the excitation source with a 1 s exposure time and 3 mW power at the sample surface. The intensity of the G band (1600 cm^{-1}) was plotted to obtain the Raman map.

2.7. In Vitro Photothermal Therapy. SKBR-3 cells incubated with GO−AuNS hybrids for 24 h were exposed to an 808 nm diode laser for different durations as described in the text. Following laser illumination, the cells were incubated with fluorescent labels of ethidium homobromide 1 and calcein AM dyes to produce green and red emission from live and dead cells, respectively, to visualize them under a fluorescence microscope. The cell viability upon treatment with the laser was also quantified using MTT assay 24 and 48 h post-treatment.

3. RESULTS AND DISCUSSION

3.1. Synthesis and Characterization of GO−AuNS Nanopatches. GO−AuNS hybrid nanopatches with tunable optical properties are synthesized according to our previous work reported elsewhere (Figure 1).[32] Owing to favored

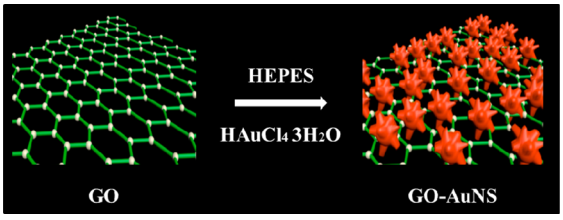

Figure 1. Scheme depicting the synthesis of AuNSs on the GO surface.

heterogeneous nucleation and consequent growth, the reduction of the Au precursor ($HAuCl_4$) using HEPES in the presence of graphene oxide resulted in the formation of AuNSs that are anchored to GO (Figure S1, Supporting Information). GO serves as a flexible soft template for surface-mediated growth of these nanostructures. HEPES enabled the reduction of $HAuCl_4$ in the aqueous phase through the oxidation of its N-substituted piperazine ring to a N-centered cationic free radical, producing gold nanostructures at room temperature and neutral pH (pH 7.4) and obviating the need for toxic reducing or growth-directing agents.[30,33] HEPES also facilitates the anisotropic growth and shape control of AuNSs along the

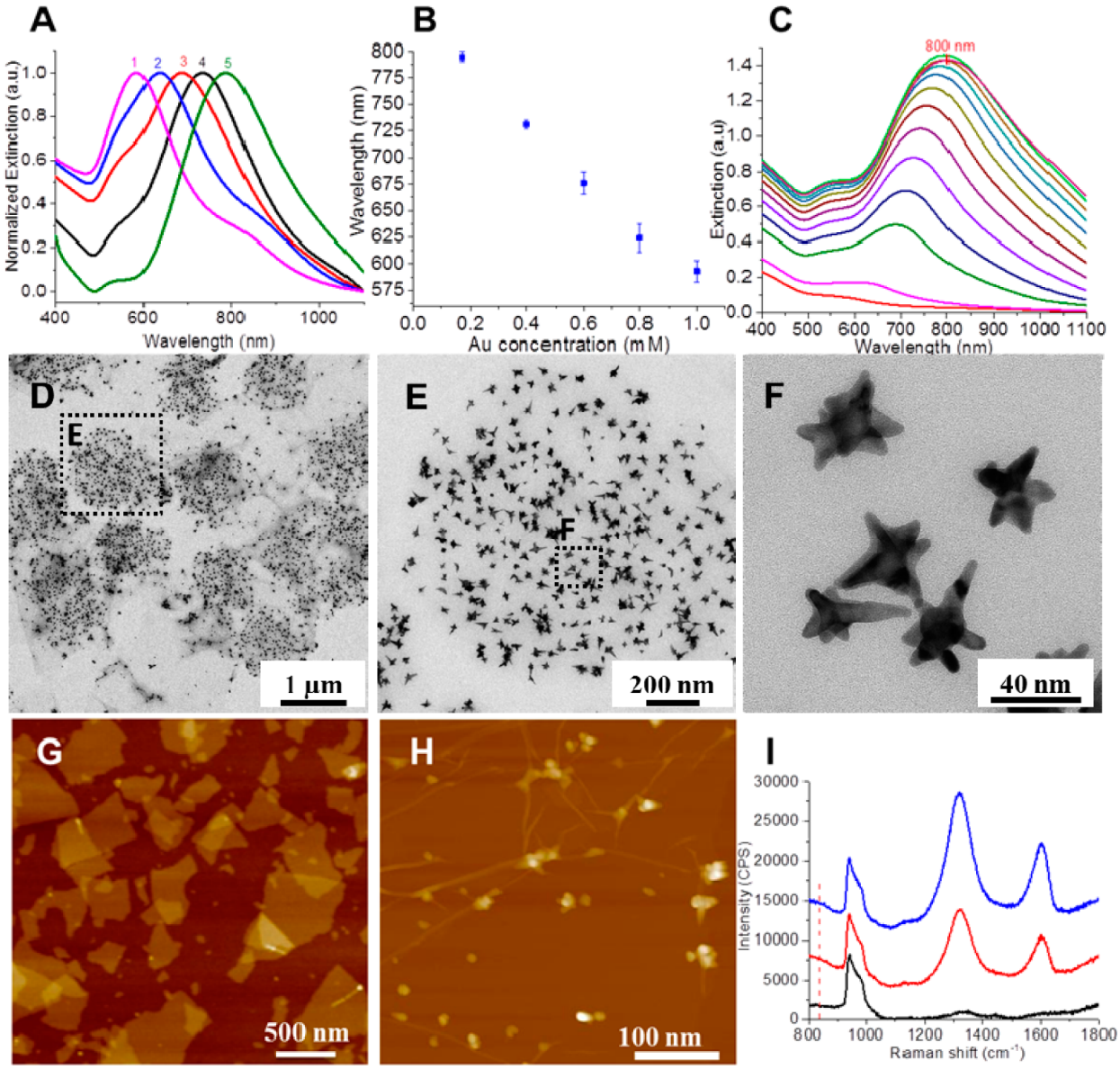

Figure 2. (A) Vis−NIR extinction spectra showing the tunable localized surface plasmon resonance of GO−AuNS hybrids. [GO] = 10 μg/mL and [Au] = 1, 0.8, 0.6, and 0.4 mM for 1−4, respectively. [GO] = 5 μg/mL and [Au] = 0.2 mM for 5. (B) Progressive blue shift in the LSPR wavelength with increasing Au concentration. (C) In situ vis−NIR extinction spectra of gold nanostar synthesis in 0.1 M HEPES using 0.2 mM Au in the presence of 5 μg/mL graphene oxide. The synthesis of GO−AuNS nanopatches is complete in 15 min. (D−F) Transmission electron microscopy images of GO−AuNS nanopatches. Atomic force microscopy image of (G) graphene oxide and (H) GO−AuNS hybrid nanopatches. The *z*-scale is 8 nm for (A) and 100 nm for (B). (I) Raman spectra of AuNSs, GO, and GO−AuNS hybrids electrostatically adsorbed onto an amine-terminated silicon surface.

⟨111⟩ direction through strong affinity of the piperazine ring for the {100} planes of gold in comparison to weak or no adsorption on the {111} planes.[30] By changing the GO to gold ratio, the density and LSPR wavelength of AuNS on GO could be tuned from visible to near-infrared (NIR) wavelength (Figure 2 A−F). Tuning the LSPR wavelength of photothermal contrast agents to the NIR therapeutic window (650−900 nm), where the endogenous absorption coefficient of tissue is nearly 2 orders of magnitude lower compared to that in the visible part of the electron microscopy (EM) spectrum, is critical to ensure light penetration into soft tissues.[34] As the GO acts as the preferred template for the nucleation and growth of the gold nanostructures, increasing the GO to Au ratio resulted in the enhanced nucleation (i.e., increased density of AuNSs on GO) and higher anisotropy (arm length) of the AuNSs, both of which result in a red shift in the LSPR wavelength.[35] For optimal photothermal transduction, the LSPR wavelength of the AuNSs was tuned to 802 ± 6 nm to match the wavelength of the diode laser (808 nm) used in this study.

Raman spectroscopy serves as a valuable tool for probing the structure and properties of nanocarbons, which are known to exhibit strong Raman scattering. Raman spectra of graphene-based nanomaterials are known to exhibit three characteristic Raman bands: graphitic (G) band (~1560−1590 cm^{-1}), defect (D) mode (~1350 cm^{-1}), and second-order defect mode (~2700 cm^{-1}).[36] Raman spectra obtained from GO−AuNS hybrids deposited on a silicon substrate revealed nearly 3-fold Raman enhancement of the D and G band intensities compared

dx.doi.org/10.1021/am504795d | *ACS Appl. Mater. Interfaces* 2014, 6, 16395−16402

to that of bare GO due to the enhanced electromagnetic field around Au nanostars that are anchored on the surface of the GO (Figure 2 G–I). Absence of a Raman band corresponding to the piperazine ring at 836 cm^{-1} indicated that GO–AuNS hybrids did not possess any detectable level of HEPES on the surface due to its weak or no affinity for the {111} planes of AuNSs.[30]

3.2. Biophysicochemical Properties. Now we turn our attention to biophysicochemical properties of the nanopatches, which are extremely important for their efficient and safe deployment in biomedical applications such as bioimaging and locoregional therapy. Many nanomaterial characteristics including size, shape, aggregation state, surface properties, and chemistry have been demonstrated to have significant correlation with their toxicity profiles when interfaced with biotic entities from the molecular to cell to organism level.[37−44] GO–AuNS hybrids exhibited excellent stability in 10% FBS over a course of 10 days (Figure S2, Supporting Informaiton). Monitoring the vis–NIR extinction spectra of plasmonic nanostructures is a convenient method to probe the serum stability of plasmonic nanostructures. A 10 nm red shift in the LSPR wavelength of AuNSs within the first 24 h indicated relatively small nonspecific adsorption of the serum proteins that is known to mitigate the cytotoxicity of the nanostructures.[45] No further red shift was observed after the first 24 h, indicating the absence of large-scale aggregation of the nanostructures over the course of 10 days. On the other hand, ligand-free AuNSs synthesized using HEPES as the reducing agent in the absence of GO exhibited strong aggregation within 24 h as evidenced by the significant broadening of the LSPR band and concomitant rise of a higher wavelength band due to irreversible serum protein adsorption or the formation of a hard corona (Figure S2). Gold nanoparticles synthesized using conventional approaches such as the Turkevich method or seed-mediated synthesis require extensive surface modification to lower cytotoxicity, improve their serum stability, and enhance cellular uptake.[46] In the absence of additional surface modification, AuNSs, in ligand-free form, exhibited poor stability in biological media (i.e., they formed large aggregates outside the cells) and poor internalization, if any (Figure S3, Supporting Information). The long-term biostability of the GO–AuNS hybrid structures can be attributed to the hydrophilic carboxyl, epoxy, and hydroxyl surface groups of GO that make GO a better choice for biomedical applications in comparison to other carbonaceous nanomaterials with low hydrophilicity such as fullerene, carbon nanotubes, and graphene.[47−49] Moreover, the high specific surface area of GO along with its planar and flexible nature essentially maximizes the interactions with biological species and mitigates the irreversible protein adsorption or the formation of a hard corona on AuNSs anchored on GO that resulted in the excellent biocompatibility of the hybrid nanopatches in a complex biological environment.[50]

ζ potential measurements revealed that GO, AuNSs, and GO–AuNS hybrids possessed a negative charge in water and a slightly reduced negative charge in serum (Figure S4, Supporting Information). The negative surface charge of GO is expected due to the carboxyl, epoxy, and hydroxyl surface functional groups.[50] While reduced graphene oxide could cause protein denaturation through strong $\pi-\pi$ interactions, the GO surface possesses chemical functionality that minimizes protein denaturation through mild electrostatic interactions.[51] Mildly negatively charged GO–AuNS hybrids can be advantageous to prevent the formation of a hard corona since most proteins present in the full medium possess a net negative charge, with a measured ζ potential of -9.13 ± 0.7 mV.[52] The concentration-dependent toxicity of the nanopatches to epithelial breast cancer cells (SKBR-3) and normal breast cells (MCF-10A) for 24 h has been examined using MTT assay (Figure 3). Both the

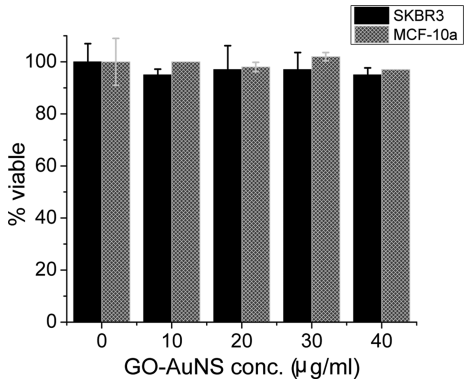

Figure 3. MTT assay showing the cell viability of SKBR-3 breast cancer cells and MCF-10a normal breast cells upon incubation with different concentrations of GO–AuNS hybrids for 24 h.

cell types maintained above 90% viability even for the highest concentration (40 μg/mL GO–AuNS hybrids) studied. Unless stated otherwise, a 10 μg/mL concentration of GO–AuNS hybrids has been used for the cellular uptake, photothermal transduction, and therapy studies and compared to the same concentrations of GO and AuNSs as controls.

3.3. Intracellular Uptake. The multifunctional nanopatches exhibited cytosolic colocalization of ligand-free, gold nanostars anchored on the surface of graphene oxide into epithelial breast cancer cells (Figure 4; Figure S5, Supporting Information). TEM of sectioned cells showed patches of

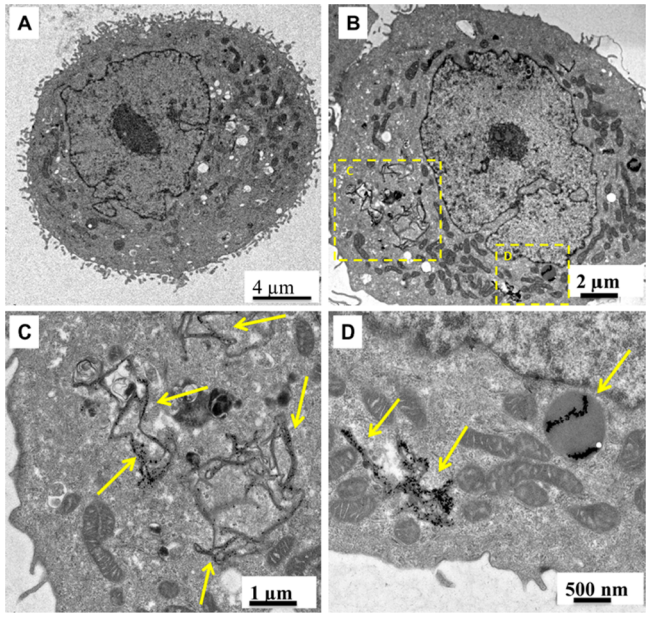

Figure 4. Internalization of GO–AuNS nanopatches into SKBR-3 cells. Tranmission electron microscopy images of (A) the sectioned SKBR-3 cells and (B–D) the sectioned SKBR-3 cells that were incubated with GO–AuNS hybrids for 24 h.

AuNSs at the interior and along the surfaces of subcellular organelles, suggesting GO and AuNS hybrids remain intact after internalization into SKBR-3 cells. The time-dependent uptake of GO−AuNS nanopatches has also been quantified using ICP-MS (Figure S6, Supporting Information).

3.4. In vitro Raman Bioimaging. Raman scattering is an attractive modality in molecular bioimaging owing to its (i) large multiplexing ability, (ii) excellent photostability compared to that of organic dyes, (iii) absence of interference from water, and (iv) high spatial resolution.[34,53−57] Raman-scattering-based in vitro imaging serves as a valuable optical imaging technique to confirm the internalization of the hybrid nanopatches.[58−60] GO is a known strong Raman scatterer which serves as a biocompatible Raman reporter, thus obviating the need for other toxic reporter molecules. Raman mapping of the graphitic (G) band of GO revealed that GO was concentrated in the cytoplasm of the cell with weak or no signal from the nucleus (Figure 5; Figures S7 and S8, Supporting Information). This is

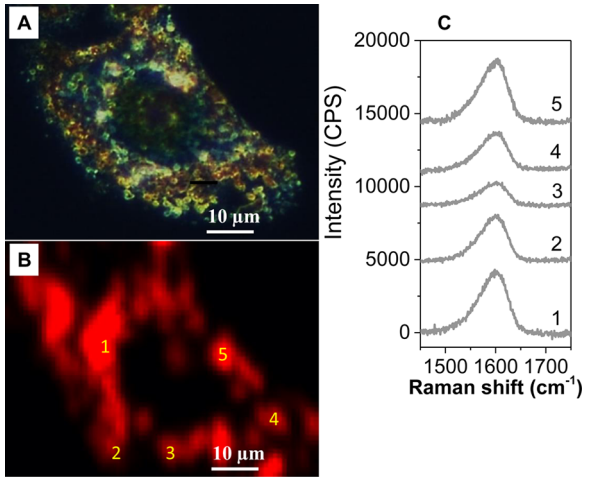

Figure 5. In vitro Raman bioimaging. (A) Dark-field scattering images of an SKBR-3 cell incubated with GO−AuNS hybrids. (B) Map of the G band (1600 cm^{-1}) intensity from a cell incubated with GO−AuNS hybrids clearly showing the presence of GO in the cytosol and absence of the same in the nucleus. (C) Representative Raman spectra obtained from various spots shown in (B).

in complete agreement with the TEM imaging, which revealed the presence of the nanopatches in the cytoplasm and their absence in the nucleus.

3.5. In Vitro Photothermal Therapy. Next, we compared the photothermal transduction capabilities of GO, AuNSs, and GO−AuNS nanopatches (Figure 6). The temperature measurements of solutions of the nanostructures showed a rapid increase for the nanopatches within 2 min of laser irradiance (laser power density of 0.75 W/cm^2) to 54.4 °C, while the same for AuNSs and GO was found to be 50 and 30 °C, respectively, under the same irradiation conditions. The temperature increase (from the room temperature of 25 °C) directly corresponds to the contribution of the individual components to the total photothermal transduction.

To monitor the therapeutic efficiency of the nanohybrids, we have performed live/dead cell assay following the irradiation of the cells with an 808 nm wavelength laser. One hour after photothermal treatment, a live/dead viability (green color for live and red color for dead) test was performed for control cells and SKBR-3 cells incubated with GO, AuNSs, and GO−AuNS

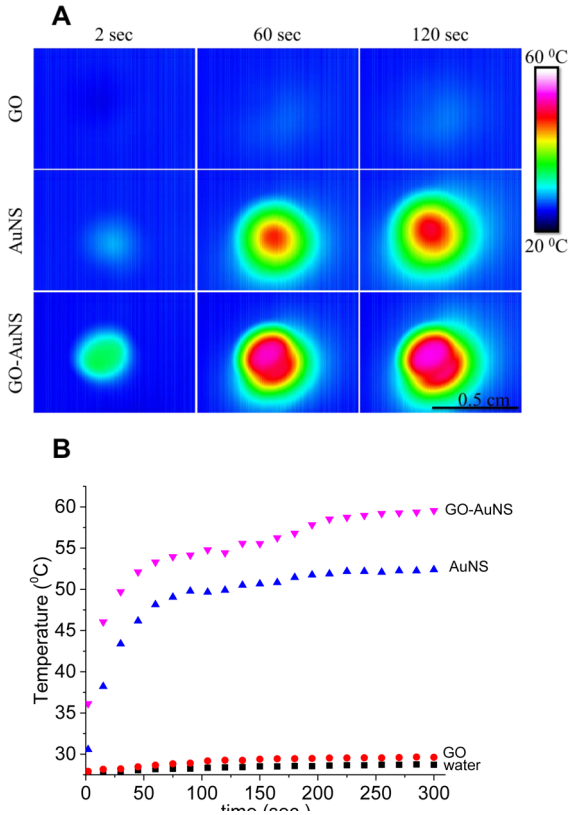

Figure 6. Photothermal efficiency of GO−AuNS nanopatches. (A) IR camera images captured from solutions of GO, AuNSs, and GO−AuNS nanopatches that were irradiated with an 808 nm laser for 2 s, 1 min, and 2 min, respectively. (B) Corresponding temperature increase of the solutions in (A).

nanohybrids. Considering the relatively low laser power density (0.75 W/cm^2), SKBR-3 cells without any GO or AuNSs maintained their healthy state as evidenced by the bright green fluorescence and the absence of red fluorescence (Figure 7A). GO and AuNSs did not cause cell death as indicated by the absence of red fluorescence, but a slight dimming in green fluorescence as compared to bright green fluorescence from the control cells suggested that GO and AuNSs caused only minor damage to the cells (Figure 7A−C). Due to its significantly low concentration (10 μg/mL), GO in the highly oxidized form of graphene has a relatively lower photothermal effect due to suboptimal absorption in the NIR range compared to graphene but offers much better biocompatibility. As opposed to individual plasmonic nanostructures that act as nanoscale heaters, the unique nanopatch-like morphology of the hybrid with a high density of AuNSs serves as a heating patch, which enhanced the local destruction of SKBR-3 cells due to their local destruction after intracellular colocalization. Furthermore, the perfect match of the LSPR wavelength of AuNSs with the excitation laser wavelength (808 nm) maximizes the photothermal effect of the nanopatch. Complete cell death occurred at ultralow power laser irradiation (0.75 W/cm^2) for 2 min of laser exposure (Figure 7D; Figure S9, Supporting Information). It should be noted that even though AuNSs have a remarkable photothermal transduction capability evidenced by the temperature measurements of the nanoparticle solutions, their negligible cellular uptake in the absence of surface modifications and aggregation outside the cells resulted in their poor therapeutic effect. This is direct evidence that GO dictates both

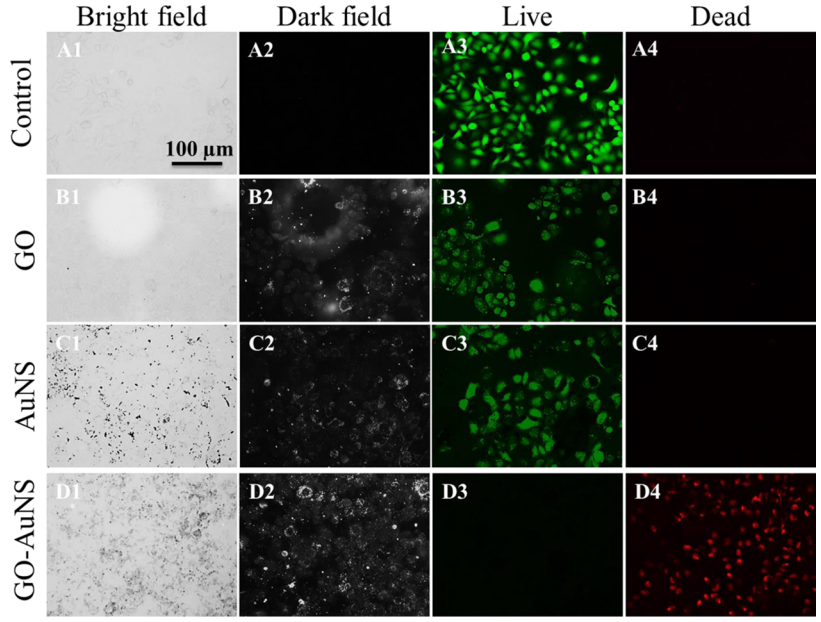

Figure 7. In vitro photothermal therapy using GO–AuNS nanopatches. Columns 1, 2, 3, and 4 are bright-field, dark-field, green fluorescence (live), and red fluorescence (dead) microscopy images, respectively. Rows A, B, C, and D are control SKBR-3 cells and cells incubated with GO, AuNSs, and GO–AuNS nanopatches and irradiated with an 808 nm laser with a power density of 0.75 W cm^{-2} for 2 min.

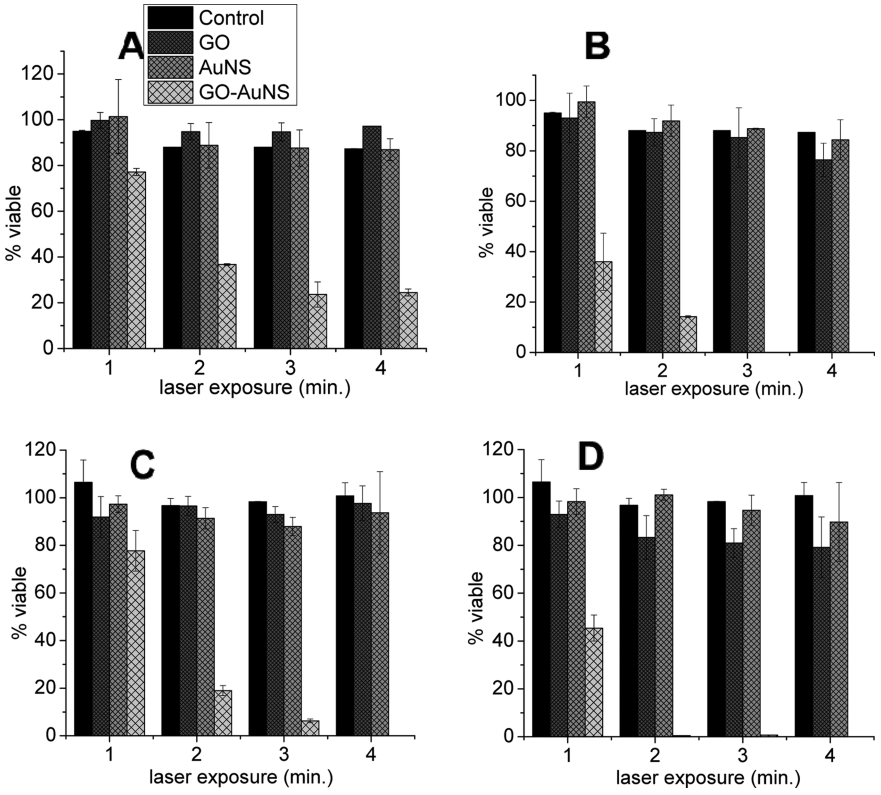

Figure 8. MTT assay for quantifying the viability of SKBR-3 cells incubated with GO–AuNS nanopatches after photothermal therapy. SKBR-3 cell viabilities upon incubation with 5 μg/mL GO–AuNS nanopatches (A) 24 h and (B) 48 h post-treatment for varied laser exposure times and with 10 μg/mL GO–AuNS nanopatches (C) 24 h and (D) 48 h post-treatment for varied laser exposure times. Note that complete cell death occurs with extended laser exposure times in (B)–(D) for GO–AuNS-nanopatch-incubated SKBR-3 cells.

the biostability and the efficient intracellular uptake and colocalization of the gold nanostars on the nanopatches, which contributed to the efficient photothermal therapy at ultralow dosages of GO, that is, at least an order of magnitude lower compared to the doses used in previous studies.[61−63]

The photothermal efficiency of GO–AuNS nanopatches was further quantified using MTT assay, which confirmed that the complete cell destruction was achieved using ultralow laser power irradiation. SKBR-3 cells incubated with 5 μg/mL GO–AuNS nanohybrids and irradiated with a laser for 2 min showed

dx.doi.org/10.1021/am504795d | ACS Appl. Mater. Interfaces 2014, 6, 16395−16402

36 ± 1% viability after 24 h and 14 ± 0.3% viability after 48 h (Figure 8A,B). SKBR-3 cells incubated with 10 μg/mL GO−AuNS hybrids and irradiated with a laser for 2 min showed a drop from 19 ± 2% viability after 24 h to complete cell death at 48 h (Figure 8C,D). Compared to GO or AuNSs alone, for which we observed 80% or higher cell viability in all cases, GO−AuNS nanopatches proved to be extremely effective for photothermal therapy.

4. CONCLUSION

Taken together, we demonstrated novel multifunctional and biocompatible hybrids of graphene oxide and metal nanostructures that hold great potential for efficacious cancer theranostics. In vivo studies are required to test and realize the nanopatches further. Understanding the underlying material factors that lead to a particular cellular uptake mechanism of the nanopatches such as amphipathic surface chemistry or the flexible mechanics of the sheet structure can shed light on better nanomedicine design, which is currently being investigated.

■ ASSOCIATED CONTENT

Supporting Information

Additional atomic force microscopy images, vis−NIR spectra, Raman images, live/dead fluorescent images, and transmission electron microscopy images of the sectioned SKBR-3 cells incubated with GO−AuNS. This material is available free of charge via the Internet at http://pubs.acs.org.

■ AUTHOR INFORMATION

Corresponding Author

*E-mail: singamaneni@wustl.edu. Phone: 314-935-5407. Fax: 314-935-4014.

Notes

The authors declare no competing financial interest.

■ ACKNOWLEDGMENTS

We acknowledge financial support from the National Science Foundation CAREER award (Grant CBET-1254399). We thank the Nano Research Facility (NRF), a member of the National Nanotechnology Infrastructure Network (NNIN), for providing access to electron microscopy facilities. We thank Prof. Lihong Wang in the Department of Biomedical Engineering at Washington University for providing access to an IR camera.

■ REFERENCES

(1) van der Zee, J. Heating the Patient: A Promising Approach. *Ann. Oncol.* **2002**, *13*, 1173−1184.
(2) Chicheł, A.; Skowronek, J.; Kubaszewska, M.; Kanikowski, M. Hyperthermia—Description of a Method and a Review of Clinical Applications. *Rep. Pract. Oncol. Radiother.* **2007**, *12*, 267−275.
(3) Dewey, W. C. Arrhenius Relationships from the Molecule and Cell to the Clinic. *Int. J. Hyperther.* **2009**, *25*, 3−20.
(4) Wust, P.; Hildebrandt, B.; Sreenivasa, G.; Rau, B.; Gellermann, J.; Riess, H.; Felix, R.; Schlag, P. M. Hyperthermia in Combined Treatment of Cancer. *Lancet Oncol.* **2002**, *3*, 487−497.
(5) Leroueil, P. R.; Hong, S.; Mecke, A.; Baker, J. R.; Orr, B. G.; Banaszak Holl, M. M. Nanoparticle Interaction with Biological Membranes: Does Nanotechnology Present a Janus Face? *Acc. Chem. Res.* **2007**, *40*, 335−342.
(6) Jain, P. K.; Huang, X.; El-Sayed, I. H.; El-Sayed, M. A. Noble Metals on the Nanoscale: Optical and Photothermal Properties and Some Applications in Imaging, Sensing, Biology, and Medicine. *Acc. Chem. Res.* **2008**, *41*, 1578−1586.
(7) Dykman, L.; Khlebtsov, N. Gold Nanoparticles in Biomedical Applications: Recent Advances and Perspectives. *Chem. Soc. Rev.* **2012**, *41*, 2256−2282.
(8) Murphy, C. J.; Gole, A. M.; Stone, J. W.; Sisco, P. N.; Alkilany, A. M.; Goldsmith, E. C.; Baxter, S. C. Gold Nanoparticles in Biology: Beyond Toxicity to Cellular Imaging. *Acc. Chem. Res.* **2008**, *41*, 1721−1730.
(9) Nergiz, S. Z.; Gandra, N.; Farrell, M. E.; Tian, L.; Pellegrino, P. M.; Singamaneni, S. Biomimetic Sers Substrate: Peptide Recognition Elements for Highly Selective Chemical Detection in Chemically Complex Media. *J. Mater. Chem. A* **2013**, *1*, 6543−6549.
(10) Doane, T. L.; Burda, C. The Unique Role of Nanoparticles in Nanomedicine: Imaging, Drug Delivery and Therapy. *Chem. Soc. Rev.* **2012**, *41*, 2885−2911.
(11) Loo, C.; Lowery, A.; Halas, N.; West, J.; Drezek, R. Immunotargeted Nanoshells for Integrated Cancer Imaging and Therapy. *Nano Lett.* **2005**, *5*, 709−711.
(12) Bardhan, R.; Lal, S.; Joshi, A.; Halas, N. J. Theranostic Nanoshells: From Probe Design to Imaging and Treatment of Cancer. *Acc. Chem. Res.* **2011**, *44*, 936−946.
(13) Alkilany, A. M.; Thompson, L. B.; Boulos, S. P.; Sisco, P. N.; Murphy, C. J. Gold Nanorods: Their Potential for Photothermal Therapeutics and Drug Delivery, Tempered by the Complexity of Their Biological Interactions. *Adv. Drug Delivery Rev.* **2012**, *64*, 190−199.
(14) Skrabalak, S. E.; Chen, J.; Sun, Y.; Lu, X.; Au, L.; Cobley, C. M.; Xia, Y. Gold Nanocages: Synthesis, Properties, and Applications. *Acc. Chem. Res.* **2008**, *41*, 1587−1595.
(15) Dreaden, E. C.; Mackey, M. A.; Huang, X.; Kang, B.; El-Sayed, M. A. Beating Cancer in Multiple Ways Using Nanogold. *Chem. Soc. Rev.* **2011**, *40*, 3391−3404.
(16) Shen, H.; Zhang, L.; Liu, M.; Zhang, Z. Biomedical Applications of Graphene. *Theranostics* **2012**, *2*, 283−294.
(17) Cha, C.; Shin, S. R.; Annabi, N.; Dokmeci, M. R.; Khademhosseini, A. Carbon-Based Nanomaterials: Multifunctional Materials for Biomedical Engineering. *ACS Nano* **2013**, *7*, 2891−2897.
(18) Antaris, A. L.; Robinson, J. T.; Yaghi, O. K.; Hong, G.; Diao, S.; Luong, R.; Dai, H. Ultra-Low Doses of Chirality Sorted (6,5) Carbon Nanotubes for Simultaneous Tumor Imaging and Photothermal Therapy. *ACS Nano* **2013**, *7*, 3644−3652.
(19) Novoselov, K. S.; Falko, V. I.; Colombo, L.; Gellert, P. R.; Schwab, M. G.; Kim, K. A Roadmap for Graphene. *Nature* **2012**, *490*, 192−200.
(20) Girish, C. M.; Sasidharan, A.; Gowd, G. S.; Nair, S.; Koyakutty, M. Confocal Raman Imaging Study Showing Macrophage Mediated Biodegradation of Graphene in Vivo. *Adv. Healthcare Mater.* **2013**, *2*, 1489−1500.
(21) Yang, K.; Feng, L.; Shi, X.; Liu, Z. Nano-Graphene in Biomedicine: Theranostic Applications. *Chem. Soc. Rev.* **2013**, *42*, 530−547.
(22) Chen, Y.; Guo, F.; Qiu, Y.; Hu, H.; Kulaots, I.; Walsh, E.; Hurt, R. H. Encapsulation of Particle Ensembles in Graphene Nanosacks as a New Route to Multifunctional Materials. *ACS Nano* **2013**, *7*, 3744−3753.
(23) Yang, K.; Wan, J.; Zhang, S.; Tian, B.; Zhang, Y.; Liu, Z. The Influence of Surface Chemistry and Size of Nanoscale Graphene Oxide on Photothermal Therapy of Cancer Using Ultra-Low Laser Power. *Biomaterials* **2012**, *33*, 2206−2214.
(24) Shi, X.; Gong, H.; Li, Y.; Wang, C.; Cheng, L.; Liu, Z. Graphene-Based Magnetic Plasmonic Nanocomposite for Dual Bioimaging and Photothermal Therapy. *Biomaterials* **2013**, *34*, 4786−4793.
(25) Park, J.-H.; von Maltzahn, G.; Ong, L. L.; Centrone, A.; Hatton, T. A.; Ruoslahti, E.; Bhatia, S. N.; Sailor, M. J. Cooperative Nanoparticles for Tumor Detection and Photothermally Triggered Drug Delivery. *Adv. Mater.* **2010**, *22*, 880−885.
(26) Yang, K.; Hu, L.; Ma, X.; Ye, S.; Cheng, L.; Shi, X.; Li, C.; Li, Y.; Liu, Z. Multimodal Imaging Guided Photothermal Therapy Using

Functionalized Graphene Nanosheets Anchored with Magnetic Nanoparticles. *Adv. Mater.* **2012**, *24*, 1868−1872.
(27) Jiang, Z.; Dong, B.; Chen, B.; Wang, J.; Xu, L.; Zhang, S.; Song, H. Multifunctional Au@Msio2/Rhodamine B Isothiocyanate Nanocomposites: Cell Imaging, Photocontrolled Drug Release, and Photothermal Therapy for Cancer Cells. *Small* **2013**, *9*, 604−612.
(28) Park, S.; Ruoff, R. S. Chemical Methods for the Production of Graphenes. *Nat. Nanotechnol.* **2009**, *4*, 217−224.
(29) Kulkarni, D. D.; Choi, I.; Singamaneni, S. S.; Tsukruk, V. V. Graphene Oxide−Polyelectrolyte Nanomembranes. *ACS Nano* **2010**, *4*, 4667−4676.
(30) Xie, J.; Lee, J. Y.; Wang, D. I. C. Seedless, Surfactantless, High-Yield Synthesis of Branched Gold Nanocrystals in HEPES Buffer Solution. *Chem. Mater.* **2007**, *19*, 2823−2830.
(31) Cho, E. C.; Zhang, Q.; Xia, Y. The Effect of Sedimentation and Diffusion on Cellular Uptake of Gold Nanoparticles. *Nat. Nanotechnol.* **2011**, *6*, 385−391.
(32) Nergiz, S. Z.; Gandra, N.; Singamaneni, S. Self-Assembled High Aspect Ratio Gold Nanostar/Graphene Oxide Hybrid Nanorolls. *Carbon* **2014**, *66*, 585−591.
(33) Chen, R.; Wu, J.; Li, H.; Cheng, G.; Lu, Z.; Che, C.-M. Fabrication of Gold Nanoparticles with Different Morphologies in HEPES Buffer. *Rare Met.* **2010**, *29*, 180−186.
(34) Qian, X.; Peng, X.-H.; Ansari, D. O.; Yin-Goen, Q.; Chen, G. Z.; Shin, D. M.; Yang, L.; Young, A. N.; Wang, M. D.; Nie, S. In Vivo Tumor Targeting and Spectroscopic Detection with Surface-Enhanced Raman Nanoparticle Tags. *Nat. Biotechnol.* **2008**, *26*, 83−90.
(35) Khoury, C. G.; Vo-Dinh, T. Gold Nanostars for Surface-Enhanced Raman Scattering: Synthesis, Characterization and Optimization. *J. Phys. Chem. C* **2008**, *112*, 18849−18859.
(36) Ferrari, A. C.; Meyer, J. C.; Scardaci, V.; Casiraghi, C.; Lazzeri, M.; Mauri, F.; Piscanec, S.; Jiang, D.; Novoselov, K. S.; Roth, S.; Geim, A. K. Raman Spectrum of Graphene and Graphene Layers. *Phys. Rev. Lett.* **2006**, *97*, 187401.
(37) Nel, A.; Xia, T.; Madler, L.; Li, N. Toxic Potential of Materials at the Nanolevel. *Science* **2006**, *311*, 622−627.
(38) Nel, A. E.; Madler, L.; Velegol, D.; Xia, T.; Hoek, E. M. V.; Somasundaran, P.; Klaessig, F.; Castranova, V.; Thompson, M. Understanding Biophysicochemical Interactions at the Nano-Bio Interface. *Nat. Mater.* **2009**, *8*, 543−557.
(39) George, S.; Lin, S.; Ji, Z.; Thomas, C. R.; Li, L.; Mecklenburg, M.; Meng, H.; Wang, X.; Zhang, H.; Xia, T.; Hohman, J. N.; Lin, S.; Zink, J. I.; Weiss, P. S.; Nel, A. E. Surface Defects on Plate-Shaped Silver Nanoparticles Contribute to Its Hazard Potential in a Fish Gill Cell Line and Zebrafish Embryos. *ACS Nano* **2012**, *6*, 3745−3759.
(40) Zhu, M.; Nie, G.; Meng, H.; Xia, T.; Nel, A.; Zhao, Y. Physicochemical Properties Determine Nanomaterial Cellular Uptake, Transport, and Fate. *Acc. Chem. Res.* **2013**, *46*, 622−631.
(41) Nergiz, S. Z.; Slocik, J. M.; Naik, R. R.; Singamaneni, S. Surface Defect Sites Facilitate Fibrillation: An Insight into Adsorption of Gold-Binding Peptides on Au(111). *Phys. Chem. Chem. Phys.* **2013**, *15*, 11629−11633.
(42) Dykman, L. A.; Khlebtsov, N. G. Uptake of Engineered Gold Nanoparticles into Mammalian Cells. *Chem. Rev.* **2014**, *114*, 1258−1288.
(43) Mu, Q.; Jiang, G.; Chen, L.; Zhou, H.; Fourches, D.; Tropsha, A.; Yan, B. Chemical Basis of Interactions between Engineered Nanoparticles and Biological Systems. *Chem. Rev.* **2014**, *114*, 7740−7781.
(44) Dobrovolskaia, M.; McNeil, S. Immunological Properties of Engineered Nanomaterials. *Nat. Nanotechnol.* **2007**, *2*, 469−478.
(45) Hu, W.; Peng, C.; Lv, M.; Li, X.; Zhang, Y.; Chen, N.; Fan, C.; Huang, Q. Protein Corona-Mediated Mitigation of Cytotoxicity of Graphene Oxide. *ACS Nano* **2011**, *5*, 3693−3700.
(46) Alkilany, A. M.; Lohse, S. E.; Murphy, C. J. The Gold Standard: Gold Nanoparticle Libraries To Understand the Nano−Bio Interface. *Acc. Chem. Res.* **2012**, *46*, 650−661.
(47) Montellano, A.; Da Ros, T.; Bianco, A.; Prato, M. Fullerene C60 as a Multifunctional System for Drug and Gene Delivery. *Nanoscale* **2011**, *3*, 4035−4041.
(48) Hu, X.; Zhou, Q. Health and Ecosystem Risks of Graphene. *Chem. Rev.* **2013**, *113*, 3815−3835.
(49) Bussy, C.; Ali-Boucetta, H.; Kostarelos, K. Safety Considerations for Graphene: Lessons Learnt from Carbon Nanotubes. *Acc. Chem. Res.* **2012**, *46*, 692−701.
(50) Gonçalves, G.; Vila, M.; Portolés, M.-T.; Vallet-Regi, M.; Gracio, J.; Marques, P. A. A. P. Nano-Graphene Oxide: A Potential Multifunctional Platform for Cancer Therapy. *Adv. Healthcare Mater.* **2013**, *2*, 1072−1090.
(51) Lee, W. C.; Lim, C. H. Y. X.; Shi, H.; Tang, L. A. L.; Wang, Y.; Lim, C. T.; Loh, K. P. Origin of Enhanced Stem Cell Growth and Differentiation on Graphene and Graphene Oxide. *ACS Nano* **2011**, *5*, 7334−7341.
(52) Xiao, K.; Li, Y.; Luo, J.; Lee, J. S.; Xiao, W.; Gonik, A. M.; Agarwal, R. G.; Lam, K. S. The Effect of Surface Charge on in Vivo Biodistribution of Peg-Oligocholic Acid Based Micellar Nanoparticles. *Biomaterials* **2011**, *32*, 3435−3446.
(53) Keren, S.; Zavaleta, C.; Cheng, Z.; de la Zerda, A.; Gheysens, O.; Gambhir, S. S. Noninvasive Molecular Imaging of Small Living Subjects Using Raman Spectroscopy. *Proc. Natl. Acad. Sci. U.S.A.* **2008**, *105*, 5844−5849.
(54) Zhang, X.; Young, M. A.; Lyandres, O.; Van Duyne, R. P. Rapid Detection of an Anthrax Biomarker by Surface-Enhanced Raman Spectroscopy. *J. Am. Chem. Soc.* **2005**, *127*, 4484−4489.
(55) Zavaleta, C. L.; Kircher, M. F.; Gambhir, S. S. Raman's "Effect" on Molecular Imaging. *J. Nucl. Med.* **2011**, *52*, 1839−1844.
(56) Zavaleta, C. L.; Smith, B. R.; Walton, I.; Doering, W.; Davis, G.; Shojaei, B.; Natan, M. J.; Gambhir, S. S. Multiplexed Imaging of Surface Enhanced Raman Scattering Nanotags in Living Mice Using Noninvasive Raman Spectroscopy. *Proc. Natl. Acad. Sci. U.S.A.* **2009**, *106*, 13511−13516.
(57) Kircher, M. F.; de la Zerda, A.; Jokerst, J. V.; Zavaleta, C. L.; Kempen, P. J.; Mittra, E.; Pitter, K.; Huang, R.; Campos, C.; Habte, F.; Sinclair, R.; Brennan, C. W.; Mellinghoff, I. K.; Holland, E. C.; Gambhir, S. S. A Brain Tumor Molecular Imaging Strategy Using a New Triple-Modality MRI-Photoacoustic-Raman Nanoparticle. *Nat. Med.* **2012**, *18*, 829−834.
(58) Gandra, N.; Singamaneni, S. Bilayered Raman-Intense Gold Nanostructures with Hidden Tags (Brights) for High-Resolution Bioimaging. *Adv. Mater.* **2013**, *25*, 1022−1027.
(59) Gandra, N.; Singamaneni, S. Surface-Enhanced Raman Scattering for in Vivo Imaging: The Future Looks Bright? *Nanomedicine* **2013**, *8*, 317−320.
(60) Drescher, D.; Kneipp, J. Nanomaterials in Complex Biological Systems: Insights from Raman Spectroscopy. *Chem. Soc. Rev.* **2012**, *41*, 5780−5799.
(61) Zhang, X.; Yin, J.; Peng, C.; Hu, W.; Zhu, Z.; Li, W.; Fan, C.; Huang, Q. Distribution and Biocompatibility Studies of Graphene Oxide in Mice after Intravenous Administration. *Carbon* **2011**, *49*, 986−995.
(62) Yang, K.; Zhang, S.; Zhang, G.; Sun, X.; Lee, S.-T.; Liu, Z. Graphene in Mice: Ultrahigh in Vivo Tumor Uptake and Efficient Photothermal Therapy. *Nano Lett.* **2010**, *10*, 3318−3323.
(63) Zhang, W.; Guo, Z.; Huang, D.; Liu, Z.; Guo, X.; Zhong, H. Synergistic Effect of Chemo-Photothermal Therapy Using Pegylated Graphene Oxide. *Biomaterials* **2011**, *32*, 8555−8561.